

CacheInf: Collaborative Edge-Cloud Cache System for Efficient Robotic Visual Model Inference

Abstract

Real-time visual model inference is crucial for various robotic tasks deployed on mobile robots in the field, but limited on-board computation power and limited and unstable wireless network bandwidth of the mobile robot constraint the speed of either local computation or offloading the computation to remote GPU servers for visual model inference; the prolonged inference time also increases energy consumption for the inference on each input. We observe operators in visual models typically compute on local geometries and consecutive inference inputs often share similar local geometries, which provides opportunity to cache and reuse computation results to accelerate both local computation and offloading.

Based on these observations, we propose CacheInf, a collaborative edge-cloud cache system for efficient robotic visual model inference. CacheInf first profiles the visual model and schedules for optimal offloading / local computation plan at different ratio of reusable cache. At runtime, it analyses the incoming inference input and manages reusable cache on both the robot and the server; then CacheInf dispatches local computation and offloading on reduced input size by reusing cached computation results both on the robot and the server, which accelerates both local computation and offloading. Evaluation on various visual models and wireless network environments shows CacheInf reduced end-to-end inference latency by up to 48.8% and reduced average energy consumption for inference on each input by up to 39.9%.

1 Introduction

Visual information is vital for various robotic tasks deployed on real-world edge devices (typically mobile robots), such as navigation [23], manipulation [3], and human-robot interaction [34]; and as a major visual information processing method, fast visual model inference is important for the real-world robotic tasks to timely respond to environment changes. Unfortunately, the mobile robots often suffer slow visual model inference, because they are typically limited in computation power and have limited and unstable wireless network bandwidth [36], making both local computation and naively offloading the computation to GPU servers slow.

To tackle this problem, we observe that introducing the classic caching mechanism into robotic visual model inference has the potential to accelerate both local computation and offloading the computation to GPU servers. It is based on the facts that the input for the robotic visual models is typically a continual stream of images and these models mostly compute on the images using local operators (i.e., operators

such as convolution that relies on local geometries of the input images) [17, 30]. In such cases, computation results of similar local geometries between consecutive images can be reused to shrink the overall size of the computation, which reduce both local computation time and transmission time when offloading computation to the GPU server.

However, the existing caching systems for visual models are designed for interactive generative image edition on high-end PCs and unfit for robotic tasks on mobile robots [8]. With their targeted scenario, they assume no perspective changes in the images, consume too much memory by caching computation results of every local operator and do not consider the acceleration opportunity of offloading the computation to other GPU servers. A new caching system specifically designed for robotic visual model inference is desired.

To fulfill this gap, in this paper, we propose CacheInf, a collaborative edge-cloud cache system for efficient robotic visual model inference. Given a continuous stream of visual input in a robotic visual task, CacheInf analyses the overlapping area between consecutive inputs; based on the portion of overlapping area (reusable cache) and the current estimated wireless network bandwidth, CacheInf schedules on the action between reusing local cache to reduce local computation time and reusing the remote cache (e.g., the cache at the GPU server side from the robot's perspective) to reduce transmission time, to ultimately reduce the overall visual model inference latency.

The design of CacheInf is non-trivial. The first challenge is to transform cached results to local computation acceleration. While the computation of cached areas can be skipped, the remaining uncached areas need computing but can not be computed on the highly optimized local operators for dense local geometries (e.g., conv2d in pytorch [18]), since these areas are typically sparse and fragmented, hindering acceleration. We designed and implemented sparse local operators based on the optimized sparse spatial data structure provided by taichi [7], which achieved comparable performance with the default local operators for dense local geometries in pytorch [18]. The computation results on sparse uncached areas can then be combined with the cache to form the correct result of the global geometry.

The second challenge is how to reduce the cache memory consumption, especially at the robot side which typically has a tight GPU memory budget. In visual models, the computation results of local operators typically consumes

significantly more memory than the parameters of local operators and naively caching all the computation results leads to heavy GPU memory burden.

We observe that in visual models, the computation result of a local operator often serves as the input of another local operator. In this case, the computation result of the sparse uncached areas of a local operator can be passed to the following local operators without loss of information, and cache between these two operators can be ignored (or merged to the first operator) to reduce memory consumption. We search for opposite to merge cache for each operator and balance between sparse computation acceleration and GPU memory consumption.

To fully exploit the potential acceleration of cache and offloading, we also integrate an emerging offloading paradigm named Hybrid-Parallel [28]: during visual model inference on an image, Hybrid-Parallel enables splitting of the input of local operators and assigns different splits to the local robot and the remote GPU server for computation, so that local computation and data transmission of one image can be parallelized to reduce inference latency. We extend the scheduler of Hybrid-Parallel to further consider the potential acceleration with cache on the robot and on the server, such that cache at both side can be fully utilized for acceleration.

We implemented CacheInf using python, pytorch [18] and taichi [7] on Ubuntu20.04. The offloading of computation is handled by the highly optimized distributed module of pytorch [21] with cuda-aware mpi backend which directly accesses GPU buffer, so as to minimize offloading overhead. Our baselines include plain local computation, a state-of-the-art computation offloading system named DSCCS [9], together with its counterpart with cache enabled modified by us, and Hybrid-Parallel [28].

We evaluated CacheInf on a four-wheel robot equipped with a Jetson NX Xavier [16] that is capable of computing locally with its low-power-consumption GPU. The offloading GPU server is a PC equipped with an Nvidia 2080ti GPU. Our datasets include the standard datasets of video frames of DAVIS [20] and CAD [4] each captured by a hand held camera and our self captured video frames using sensors on our robot. Extensive evaluation on various visual models and wireless network bandwidth circumstances shows that:

- CacheInf is fast. Among the baselines, CacheInf reduced the end-to-end inference time by 13.1% to 48.8%.
- CacheInf saves energy. Among the baselines, CacheInf reduced the average energy consumed to complete inference on each image by 9.5% to 39.9%.
- CacheInf is also memory-efficient. The above advantages were obtained by only incurring 3.2% to 64.6% increase in memory consumption for CacheInf, while naively caching the computation results of every local operator incurred 22.0% to 761.5% increase in memory consumption.

The major contribution of this paper is our new edge-cloud collaborative caching paradigm to accelerate robotic visual model inference, which reuses cached computation results to both accelerate local computation and computation offloading to remote GPU servers. The resulting system, CacheInf, collaboratively considers and reuses cached computation results on both the robot and the server and schedules the computation and offloading to minimize visual model inference latency. The accelerated visual model inference and the reduced power consumption will make real-world robots more performant on various robotic tasks and nurture more visual models to be deployed in real-world robots. The source code and evaluation logs of CacheInf is available at https://github.com/aspol2025_53/CacheInf.

The rest of the paper is organized as follows. Chapter two introduces background and related work. Chapter three gives an overview of CacheInf and Chapter four presents its detailed design. Chapter five describes implemented. Chapter six presents our evaluation results and CacheInf seven concludes.

2 Background

2.1 Vision tasks on robots

Vision tasks play a crucial role in enabling robots to perceive, understand, and interact with their environment. Visual information is essential for various robotic tasks, such as object recognition [6], navigation [23], manipulation [3], and human-robot interaction [34]. The rapid advancements in machine learning, particularly deep learning, have revolutionized the field of computer vision and have been widely adopted in robotic applications, which form the foundation for many high-level robotic tasks.

However, the deployment of visual models on resource-constrained robots poses significant challenges. Visual models often require significant computational resources and memory, which may not be readily available on robots, especially in mobile and embedded systems. Furthermore, real-time performance is critical for many robotic tasks, as robots need to process and respond to visual information quickly to ensure safe and effective operation. Therefore, fast visual model inference becomes a key requirement for the successful deployment of deep learning models in robotic applications. Addressing these challenges is essential for enabling robots to effectively perceive, understand, and interact with their environment in real-time, paving the way for more intelligent and autonomous robotic systems.

2.2 Visual Models

Convolutional layers [17] have become a fundamental building block in visual models, leading to significant breakthroughs in various computer vision tasks. Inspired by the biological structure of the visual cortex [30], these layers apply

learnable filters to the input image, performing convolution operations to produce feature maps that highlight the presence of specific patterns at different spatial locations. This enables deep learning models to capture translation-invariant features and learn hierarchical representations [11], with early layers learning low-level features like edges and corners, and deeper layers learning more complex patterns and object parts. As a result, deep convolutional neural networks (CNNs) have achieved state-of-the-art performance in various vision applications, image classification [24], object detection [6], and semantic segmentation [32], due to their ability to effectively capture and learn spatial hierarchies of features from raw input images. As the field of computer vision continues to evolve, convolutional layers are expected to remain a crucial component in the development of advanced models for understanding and analyzing visual data.

Notice that operators for DNN layer (e.g., convolution, ReLU, softmax) can be categorized into two types: local operators and global operators, depending on whether they can be computed independently with partial input according to [28], and the convolutional layer is a typical local operator, as it can be computed with partial input tensor (the blocks in the input tensor for convolution).

2.3 Resource Limitations of Robots

In real-world scenarios, robots often navigate and move around to perform tasks such as search and exploration. While wireless networks provide high mobility, they also have limited bandwidth, which can significantly impact the performance of robotic IoT systems. Wireless transmission of robots is constrained by limited bandwidth, both due to the theoretical upper limit of wireless transmission technologies and the practical instability of wireless networks. For instance, the most advanced Wi-Fi technology, Wi-Fi 6, offers a maximum theoretical bandwidth of 1.2 Gbps for a single stream [10]. However, the limited hardware resources on robots often prevent them from fully utilizing the potential of Wi-Fi 6 [36]. Moreover, the actual available bandwidth of wireless networks is often reduced in practice due to various factors, such as the movement of devices [12, 19], occlusion by physical barriers [5, 26], and preemption of the wireless channel by other devices [2, 25].

To demonstrate the instability of wireless transmission in real-world situations, we conducted a robot surveillance experiment using four-wheel robots navigating around several given points at 5-40cm/s speed in our lab (indoors) and campus garden (outdoors), with hardware and wireless network settings as described in Sec. 6.6. We saturated the wireless network connection with iperf [1] and recorded the average bandwidth capacity between these robots every 0.1s for 5 minutes.

The results in Fig. 1 show average bandwidth capacities of 93 Mbps and 73 Mbps for indoor and outdoor scenarios,

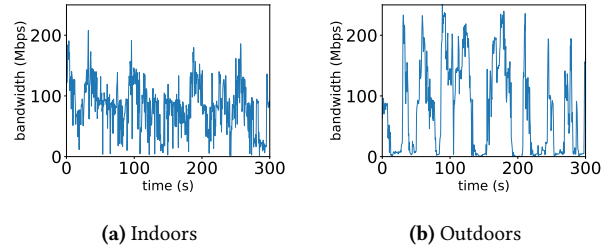


Figure 1. The instability of wireless transmission between our robot and a base station in robotic IoT networks.

respectively. The outdoor environment exhibited higher instability, with bandwidth frequently dropping to extremely low values around 0 Mbps, due to the lack of walls to reflect wireless signals and the presence of obstacles like trees between communicating robots, resulting in fewer received signals compared to indoor environments. This limitation on the bandwidth of robots' wireless network poses significant challenges for the efficient and reliable operation of robots in real-world scenarios, particularly in outdoor environments where the instability of wireless networks is more pronounced.

2.4 Related Work

Collaborative Inference expedites the overall inference process by leveraging a GPU server to handle a portion of the computational workload. While the DSCCS approach [9] focuses on model layer-level scheduling (layer partitioning) for rapid inference, Hybrid-Parallel [28] offers a more fine-grained control by scheduling at the local operator level, enhancing parallelism and further accelerating inference. However, despite the advancements in Hybrid-Parallel techniques, the limited bandwidth still poses a bottleneck for data transmission, which our caching mechanism effectively mitigates, resulting in a significant improvement in inference performance.

3 System Overview

3.1 Working Environment

We assume that the working environment of CacheInf is a mobile robot performing robotic tasks in a real-world field which requires seamless real-time visual model inference on the continuous image stream captured from the on-board camera, to achieve real-time response to various environment changes. The robot itself is equipped with low-power-consumption gpu to perform visual model inference which is slow and consumes too much power; it has wireless network access to a remote powerful GPU server that provides opportunity of acceleration, but the connection suffers from limited and unstable wireless network bandwidth.

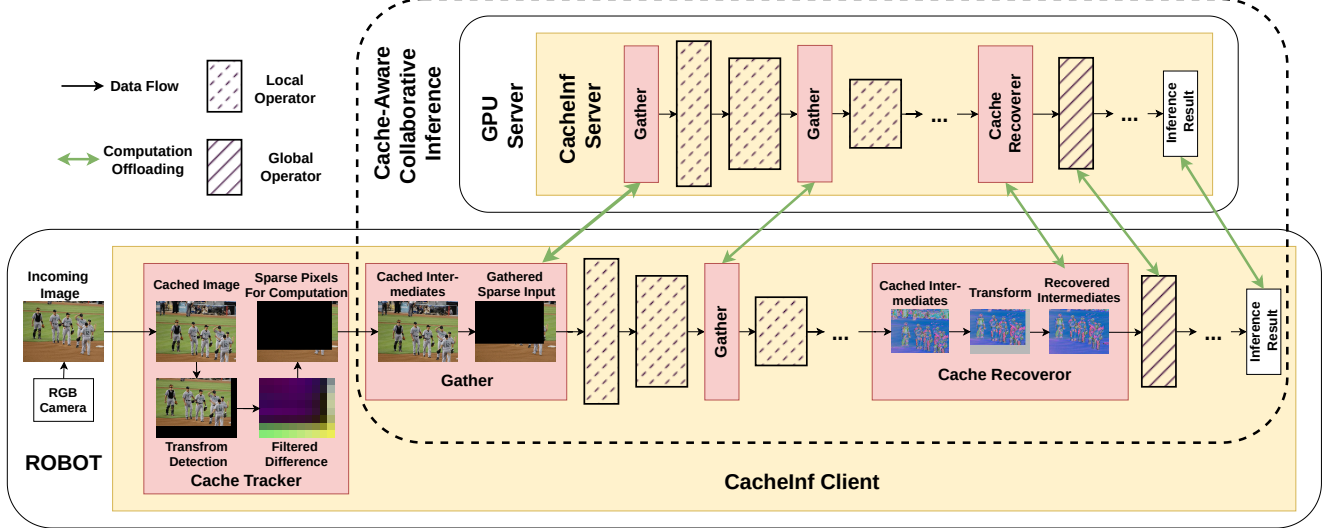


Figure 2. Architecture and workflow of CacheInf.

3.2 Architecture of CacheInf

CacheInf consists of four major components: CacheInf Scheduler, Cache Tracker, Cache-Aware Collaborative Inference and Cache Recoverer. CacheInf Scheduler functions at the initialization stage and we exclude it in Figure 2 which describes the runtime of CacheInf for simplicity.

3.2.1 CacheInf Scheduler. During the initialization stage of the robotic task and CacheInf is granted access to a visual model and an initial input image. CacheInf Scheduler first profiles the visual model based on this initial input and its execution statistics on both the robot and the server. Then it decides on the set of operators involved in the visual model that should cache their computation results and computes for an optimized computation and offloading plan for each possible situation including different wireless network bandwidth and different ratio of reusable cache.

3.2.2 Cache Tracker. Given a pair of consecutive image inputs and the former one’s computation intermediates at the selected operators are cached, Cache Tracker identifies the reusable portion of these computation intermediates. We use the standard image stitching method to try to stitch as large as possible area of the two images, which results in a perspective transform that maps the pixels from the former image to the latter. And the same perspective transform can be applied to the cached computation results since they are computed by local operators that keep the local geometries of the input image. We then filter the difference between the mapped pixel pairs and find areas of similar appearance whose correspondent cache is reusable. Pixels from uncached areas are finally gathered for computation. Note that the computation involved in this process is light-weight

compared with the visual model inference that typically involves hundreds of operators.

3.2.3 Cache-Aware Collaborative Inference and Cache Recoverer.

In this stage, we select a precomputed plan based on the current estimated wireless network bandwidth and the estimated ratio of reusable cache and execute it at both the robot and the server. We pass the gathered sparse pixels that need computation through the sequence of operators involved in the visual model. When a local operator with cache is met, we gather (depicted in Gather in Figure 2) extra pixels from cache and form correct input (e.g., wrap around a pixel into a 5x5 pixel block for a convolution kernel with size 3, detailed in Section 4.2) and feed it to the corresponding sparse local operator and subsequently the following local operators whose cache is merged. Offloading computation and receiving computation result of local operators between the robot and the server only happens at local operators with cache because they can gather extra pixels required by the computation of the opportunity side, where we slice the gathered input into splits at the planned ratio and assign them to the robot and the server.

When a first non-local operator (e.g., linear, flatten) is met, Cache Recoverer transforms the cached output of the previous local operator and merges it with the current computation result on the sparse pixels to recover the global geometry for subsequent computation.

4 Design

This chapter presents the detailed design for CacheInf to fulfill the functionality of tracking and reusing cached computation results and scheduling for actions among local computation, offloading or hybrid, with or without cache, to

optimally reduce visual model inference latency for mobile robots.

4.1 Identifying Reusable Computation Results

To find and match similar local geometries between consecutive images in a stream of images $\mathbf{I} = \{I_1, I_2, \dots, I_n\}$ to identify reusable cache, we use the standard image stitching procedure: given a pair of consecutive images I_j and I_{j+1} , their key points and key point descriptors (or feature vectors) are computed and matched within a distance threshold of the feature vectors; then a homography matrix M is computed based on the corresponding relationship between the key points on each image which minimizes the error. The resulting homography matrix is then used to apply perspective transformation to each pixel in I_j to form a new image \hat{I}_{j+1} closest to I_{j+1} as shown in Equation 1, where (u_j, v_j) and $(\hat{u}_{j+1}, \hat{v}_{j+1})$ and pixel indices on I_j and \hat{I}_{j+1} . It is also depicted in the Feature Based Transformed Image in Fig. 2. Since the computation of local operators relies on local geometries, the same transformation can be applied to intermediate computation results of the following local operators.

$$(\hat{u}_{j+1}, \hat{v}_{j+1}, 1) = M \times (u_j, v_j, 1) \quad (1)$$

While the above process minimizes error between \hat{I}_{j+1} and I_{j+1} , the remaining difference between them are the areas of new information which are uncached and needed to be recomputed. We filter and identify these areas by applying average pooling over the difference between \hat{I}_{j+1} and I_{j+1} and the pixels with computed difference greater than a preset threshold N (default to be 0.1 when we normalize the value of each channel of a pixel to between 0 and 1) will be marked as needed to be recomputed as in Equation 2, where u, v are the pixel indices.

$$\mathbf{uv} = \{(u, v) | \text{AveragePooling}(|\hat{I}_{j+1} - I_{j+1}|)^{u,v} \geq N\} \quad (2)$$

Suppose there are Q pixels in \mathbf{uv} and $H \times W$ total pixels in each image, we define the cache ratio between I_j and I_{j+1} as $r = \frac{Q}{H \cdot W}$.

4.2 Sparse Local Operators

From the above discussion, we have identified the pixels needed to recompute \mathbf{uv} and we suppose their corresponding features f_{inp} are of size $B \times C_1 \times Q$, along with the cached input defined as I'_{inp} of size $B \times C_1 \times H \times W$. Now we focus on how to compute the correct results based \mathbf{uv} , f_{inp} and I'_{inp} . There are mainly two kinds of local operators: element-wise local operators such as addition, subtraction, multiplication and division, which solely depends on the value of each element; and convolution local operators such as convolution, average pooling and max pooling, which is influenced by the surrounding areas (e.g., a 2D kernel) of each element. We mainly focus on the latter type of local operators since the element-wise local operators can be viewed as a special

case of convolution local operators where the surrounding area is of size one.

We first consider the scenario with dense input. Assume an image (or feature map) I_{inp} of size $B \times C_1 \times H \times W$, a convolution local operator K with its kernel sized $C_2 \times C_1 \times K_1 \times K_2$, stride 1 and no padding and its output feature map I_{out} of size $B \times C_2 \times H' \times W'$, then each of the value of the output feature map is determined by

$$I_{out}^{i,j,k,l} = \sum_{c=1}^{C_1} \sum_{m=1}^{K_1} \sum_{n=1}^{K_2} K^{j,c,m,n} * I_{inp}^{i,c,k+m-1,l+n-1}, \quad (3)$$

Omitting the batch dimension and the channel dimension (first two dimension) of I_{out} , we can learn from Equation 3 that an output value is determined by an area of $K_1 \times K_2$ on I_{inp} and we define pixels in this area as

$$P_{k,l} = \{(u, v) | k \leq u < k + K_1 \wedge l \leq v < l + K_2\} \quad (4)$$

where (k, l) is the pixels indices on I_{out} .

Moving to the sparse scenario, the indices of pixels on I_{out} that have updated value with \mathbf{uv} as input would be

$$\mathbf{uv}' = \{(k, l) | \exists P_{k,l}, s.t. P_{k,l} \cap \mathbf{uv} \neq \emptyset\} \quad (5)$$

which can be view as wrapping around pixels in \mathbf{uv} by $K_1 \times K_2$ and may involve pixels in I'_{inp} .

Note that \mathbf{uv} and cached input I'_{inp} are possibly in different planes determined by the homography matrix M . We may transform the cached intermediates every time before computation, but it will unfortunately involve computation of the whole feature map and invalidate the acceleration of sparse computation. Instead, during computation we query the original cached intermediates by transforming the pixel indices with M :

$$F(i, j, u, v, I'_{inp}, f_{inp}) = \begin{cases} f_{inp}^{i,j,u,v}, & (u, v) \in \mathbf{uv}, \\ I'_{inp}^{i,j,G(u,v,M)}, & (u, v) \notin \mathbf{uv} \end{cases} \quad (6)$$

where $G(u, v, M) = H^{-1}(M^{-1} \times H((u, v)))$ which transforms (u, v) into the plane of cached input I'_{inp} , and $H(\cdot)$ and $H^{-1}(\cdot)$ means turning a vector to a homogeneous vectors and the opposite. Then for $(u, v) \in \mathbf{uv}'$, the corresponding computed output is

$$f_{out}^{i,j,u,v} = \sum_{c=1}^{C_1} \sum_{m=1}^{K_1} \sum_{n=1}^{K_2} K^{j,c,m,n} \cdot F(i, c, k+m-1, l+n-1, I'_{inp}, f_{inp}) \quad (7)$$

Until now we get the indices of the altered output values in output feature map \mathbf{uv}' and the corresponding features f_{out} which can then be passed to the subsequent computation.

Along the local operators where local geometries are preserved, we can repeat the above process by passing only the sparse features and their indices and do not need to merge the sparse features with cache. When a non-local operator is met (e.g., matrix multiplication), we transform its cached input with M and merge f_{inp} into the transformed input according to their sparse indices \mathbf{uv} , which recovers the correct

geometries of the whole feature map. To minimize performance impact to update I'_{inp} , we update I'_{inp} by transforming I'_{inp} and merge it with f_{inp} only after the whole computation process finishes, when the system is typically idle and waiting for the next input.

Also, to save memory consumption of cached intermediates, notice that the above process is basically wrapping the sparse pixels with the kernel size $K_1 \times K_2$ and computing on the wrapped pixels, we can merge the query process in Equation 6 of multiple convolution local operators into the first convolution local operator. For example, if a next operator is a convolution local operator with kernel size $K'_1 \times K'_2$, we can wrap the sparse pixels with an extended kernel size $(K_1 + K'_1) \times (K_2 + K'_2)$ in the first local operator, and the wrapping process of the next operator is skipped (we refer to this process as merging cache). In this case, the cache for the input of the next operator is needless and can be excluded to save memory consumption and the reduced number of cached input further leverages the cost to update I'_{inp} .

4.3 Cache-Aware Scheduling

We define all the operators involved in a visual model as $\mathcal{O} = \{o_1, o_2, \dots, o_n\}$ and the portion of locally executed input of each operator as $\mathbf{X} = \{x_1, x_2, \dots, x_n\}$, $0 \leq x_i \leq 1$ and $1 - x_i$ represents the the portion of input executed on the GPU server. The indices of local operators is defined as \mathcal{O}_l . While offloading, we transmit the sparse features together with their indices encoded as a bit-mask and the transmission volume is almost inversely proportional to cache ratio r .

However, the local computation time acceleration with sparse local operators has a complex relationship with cache ratio, which is affected by the operator implementation, gpu structure and so on. Thus we profile such relationship by altering the cache ratio and x_i and record the average execution time for every operator involved in the visual model and we define the profile result as a function $T_c(o_i, x_i, r)$ for the robot (c means client) and $T_s(o_i, x_i, r)$ for the server, which returns the execution time of operator o_i under x_i with cache ratio r . We also profile the time cost to update cached input for each local operator and get $U_r(o_i, x_i, r)$ and $U_s(o_i, x_i, r)$. Note that for non-local operators ($\mathcal{O}_{nonlocal} = \{i | 1 \leq i \leq n \wedge i \notin \mathcal{O}_l\}$), we make both $T(\cdot)$ and $U(\cdot)$ returns time of computation on the whole input.

4.3.1 Schedule to Merge Cache. With the above setup, the first problem to solve will be the choices of merging the cache of sparse local operators to further accelerate computation while saving memory consumption. We define the indices of the chosen operators to cache their input as $\hat{\mathcal{O}}_c$ and the resulting reduction of cache ratio (since extra input will be included) of each operator as o_l to be $R(\hat{\mathcal{O}}_c, o_l)$. Since these choices will determine the operators that will cache their input and will be reused across different inference, these choices should be fixed during the whole inference task. Thus

we start by considering only the worst case where offloading is not possible and $\forall x_i \in \mathbf{X}, x_i = 1$. In this case the execution time of every operator will be $T_c(o_i, 1, r - R(\hat{\mathcal{O}}_c, o_i))$, and the optimization problem will be

$$\min_{\hat{\mathcal{O}}_c \subset \mathcal{O}_l} \frac{1}{w} \sum_{i=1}^n \sum_{j=0}^w T_c(o_i, 1, r_j + R(\hat{\mathcal{O}}_c, o_i)) + U_{sum}(\hat{\mathcal{O}}_c, r_j) \quad (8)$$

where $r_j = \frac{j}{w}$ with $w > 1$ is the possible cache ratio considered (we empirically set w to 10), and $U_{sum}(\hat{\mathcal{O}}_c, r) = \sum_{k \in \hat{\mathcal{O}}_c} U(o_k, x_k, r)$ is the total time to update cache of operators in $\hat{\mathcal{O}}_c$.

Solving of this optimization problem seeks the optimal choices of cache operators $\hat{\mathcal{O}}_c$ that minimizes local execution time averaged across all possible cache ratio. Note that we do not need to explicitly consider memory consumption because the latter term in Equation 8 will naturally reduce the number of cached operators and favor operators with smaller size of input and thus shorter time to update cache.

4.3.2 Schedule of Offloading. Finally, we are combining all the above components to schedule for computation and offloading in a cache-aware way to optimize end-to-end inference latency for robotic visual models. With Hybrid-Parallel integrated, cache can exists partially both at the robot and the server and we analyze the cache ratio on robot r_c and the cache ratio r_s on server by enquiry the current cached pixels with the previous slice of input (i.e., x_i). For an x_i , we define the minimum portion of locally executed input of its parent operators (i.e., operators whose output is the input of o_i) as x'_i and different between x_i indicates offloading to/from the server. For every operator $o_i \in \mathcal{O}$ involved in a visual model, we define its finishing time since the first operator starts executing as t_i^c on the robot (c means client) and t_i^s on server.

We can have the finish time of each operator on the robot and the server as the following, where $D(o_i, x'_i - x_i, r)$ is the data volume needed to be transmitted at operator o_i with cache ratios r_c and r_s and b is the estimated bandwidth:

$$t_i^c = \begin{cases} t_{i-1}^c + T_c(o_i, x_i, r_c - R(\hat{\mathcal{O}}_c, o_i)), & 1 \leq i \leq n \wedge x_i \leq x'_i \\ \max(T_c(o_i, x_i, r_c - R(\hat{\mathcal{O}}_c, o_i)) + \\ t_{i-1}^c, \frac{1}{b} D(o_i, x'_i - x_i, r) + t_i^s), & 1 \leq i \leq n \wedge x_i > x'_i \end{cases}$$

$$t_i^s = \begin{cases} t_{i-1}^s + T_s(o_i, 1 - x_i, r_s - R(\hat{\mathcal{O}}_c, o_i)), & 1 \leq i \leq n \wedge x_i \geq x'_i \\ \max(T_s(o_i, 1 - x_i, r_s - R(\hat{\mathcal{O}}_c, o_i)) + \\ t_{i-1}^s, \frac{1}{b} D(o_i, x'_i - x_i, r_s) + t_i^c), & 1 \leq i \leq n \wedge x_i < x'_i \end{cases}$$

The first rows of the above two equations describe the scenarios where either the robot or the server does not need to receive data from the opposite side and thus the finishing time of this operator only depends on its local execution

time. The second rows instead describe the opposite scenarios, where either the robot or the server needs to receive data from the opposite side (e.g., $x_i > x'_i$ for the robot) and have to wait until the same operator to finish computing at the opposite side and then be transmitted at bandwidth b .

With the above statements, optimizing the end-to-end inference latency for the visual model with cache enabled at a given bandwidth b and cache ratios r_c and r_s is to solve

$$\begin{aligned} \min_{\mathbf{x}} & t_n^c \\ \text{s.t. } & x_1 = x_n = 1 \\ & \forall j \in \mathcal{O}_{nonlocal}, x_j \pmod{1} = 0 \\ & \forall j \notin \hat{\mathcal{O}}_c, x_j = x'_j \end{aligned} \quad (9)$$

In Equation 9, the first two constraints ensure that inference output will finally be located at the robot and non-local operators will always have full input; the third constraint ensures that offloading will not happen within an operator whose cached is merged into the cache of other operators, since we cannot recover the operator's whole feature map. We solve both optimization problems in Equation 8 and 9 with the differential evolution algorithm [22] and store the solutions of different bandwidth and cache ratios of Equation 9 in a dictionary referred to as *Schedule*.

The resulting algorithms of CacheInf at both the robot and the server are presented in Algorithm 1 and Algorithm 2. Line 1 to 3 in Algorithm 1 and Line 1 to 4 in Algorithm 2 profile the model at both the robot and the server and compute a schedule as described in Section 4.3.2, where the computation is located on the server to speed up computation. The rest of Algorithm 2 is basically mirrored from that of Algorithm 1 and thus we focus on Algorithm 1 for simplicity.

Line 6 to 8 in Algorithm 1 identifies the reusable cache by matching features between the input image I and its cached counterpart $Cache[1]$ and gets the homography matrix M and the sparse uncached input that needs to be recomputed. After communicating info of bandwidth, cache ratio and homography matrix with the server, we query the *Schedule* to get input ratio x and parent operator input ratio x' as described in Section 4.3.2. Then we start executing each operator o_i involved in the model sequentially. We recover the whole input by combining sparse input inp with cache for non-local operators or gather extra pixels from cache for inp for sparse local operator computation at cached operators at line 12 to 19. When offloading is required to accelerate inference, we send a slice of inp to the server or merge received partial input from the server to inp at line 20 to 26. When inp is finally ready and not empty, we execute the operator o_i with inp where we choose the sparse local operator for sparse input and choose the original operator for dense input at line 27 to 34.

Algorithm 1: CacheInfClient

Input: A continual sequence of video images I ; DNN model M
Output: The inference results ret on each image in I

```

// profile
1  $T_c, U_c = Profile(M)$ 
2  $Send(M, T_c, U_c)$ 
3  $Schedule, \hat{\mathcal{O}}_c = Receive()$ 
4  $Cache = InitCache(\hat{\mathcal{O}}_c)$ 
    // inference
5 foreach  $I$  in  $I$  do
6      $b = EstimateBandwidth()$ 
7      $r_c, r_s = AnalyzeCacheRatio(I, Cache[1])$ 
8      $inp, M = IdentifyCache(I, Cache[1])$ 
9      $Send(b, r_c, r_s, M)$ 
10     $x, x' = Schedule[b, r_c, r_s]$ 
11    foreach  $i = 1, 2, \dots, n$  do
12        if  $i \in \mathcal{O}_{nonlocal}$  and  $x_i > 0$  and  $IsSparse(inp)$ 
13            then
14                 $inp = DenseRecover(inp, Cache[i], M)$ 
15                 $UpdateCache(Cache[i], inp, M)$ 
16        end
17        else if  $x'_i > 0$  and  $i \in \hat{\mathcal{O}}_c$  then
18             $inp = SparseGather(inp, Cache[i], M)$ 
19             $UpdateCache(Cache[i], inp, M)$ 
20        end
21        if  $x_i < x'_i$  then
22             $inp, inp' = Slice(inp, x_i, x'_i)$ 
23             $Send(inp')$ 
24        end
25        else if  $x_i > x'_i$  then
26             $inp = Merge(inp, Receive())$ 
27        end
28        if  $x_i > 0$  then
29            if  $IsSparse(inp)$  then
30                 $inp = SparseExecute(o_i, inp)$ 
31            end
32            else
33                 $inp = Execute(o_i, inp)$ 
34            end
35        end
36         $ret[I] = inp$ 
37    end
38 return  $ret$ 

```

5 Implementation

We implemented CacheInf with python, pytorch [18] and taichi [7] on Ubuntu20.04. The communication library used is the distributed module [21] of pytorch with mpi backend.

Algorithm 2: CacheInfServer

```

// profile and compute schedule at the server
1  $M, T_c, U_c = \text{Receive}()$ 
2  $T_s, U_s = \text{Profile}(M)$ 
3  $\text{Schedule}, \hat{O}_c = \text{ComputeSchedule}(T_s, U_s, T_c, U_c)$ 
4  $\text{Send}(\text{Schedule}, \hat{O}_c)$ 
5  $\text{Cache} = \text{InitCache}(\hat{O}_c)$ 
// inference
6 while True do
7    $b, r_c, r_s, M = \text{Receive}()$ 
8    $x, x' = \text{Schedule}[b, r_c, r_s]$ 
9   foreach  $i = 1, 2, \dots, n$  do
10    | if  $i \in O_{\text{nonlocal}}$  and  $x_i < 1$  and IsSparse(inp)
11    | |  $inp = \text{DenseRecover}(inp, \text{Cache}[i], M)$ 
12    | |  $\text{UpdateCache}(\text{Cache}[i], inp, M)$ 
13    | end
14    | else if  $x'_i < 1$  and  $i \in \hat{O}_c$  then
15    | |  $inp = \text{SparseGather}(inp, \text{Cache}[i], M)$ 
16    | |  $\text{UpdateCache}(\text{Cache}[i], inp, M)$ 
17    | end
18    | if  $x_i > x'_i$  then
19    | |  $inp, inp' = \text{Slice}(inp, x_i, x'_i)$ 
20    | |  $\text{Send}(inp')$ 
21    | end
22    | else if  $x_i < x'_i$  then
23    | |  $inp = \text{Merge}(inp, \text{Receive}())$ 
24    | end
25    | if  $x_i < 1$  then
26    | | if IsSparse(inp) then
27    | | |  $inp = \text{SparseExecute}(o_i, inp)$ 
28    | | end
29    | | else
30    | | |  $inp = \text{Execute}(o_i, inp)$ 
31    | | end
32    | end
33  end
34 end

```

We compiled pytorch with cuda-aware mpi enabled so that the mpi backend can directly read and write to cuda buffer to minimize communication overhead. We use mpi backend instead of the popular nccl backend because nccl is unavailable on the Jetson robot we used due to structural limitation [15].

The sparse local operators were implemented based on the bitmasked sparse nodes in taichi [7], which efficiently manages the sparse pixels in a grid and preserves the spatial structure of the sparse pixels by organizing them in a tree structure. With the spatial structure preserved, common optimization methods for cuda operators based on computation

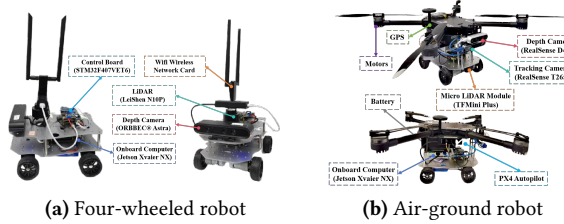


Figure 3. The composition of the four-wheeled robot and the air-ground robot used in our evaluation.

locality such as block shared memory [14] can be introduced to accelerate computation; our implemented sparse local operators achieved comparable performance with the original pytorch operators with the same input size.

6 Evaluation

6.1 Evaluation Settings

Testbed. We conducted experiments on a four-wheeled robot (Fig 3a) and a air-ground robot(Fig 3b). Both robots are equipped with a Jetson Xavier NX [16] 8G onboard computer with cuda acceleration capability and a MediaTek MT76x2U USB wireless network interface card for wireless connectivity. The Jetson Xavier NX is connected to a Leishen N10P LiDAR, an ORBBEC Astra depth camera and an STM32F407VET6 controller via USB serial ports, which are managed and driven using ROS Noetic. The GPU server used in our experiments is equipped with an Intel(R) i5 12400f CPU @ 4.40GHz and an NVIDIA GeForce GTX 2080 Ti 11GB GPU, connected to our robot via Wi-Fi 6 over 80MHz channel at 5GHz frequency.

Workload. We chose two real-world visual robotic applications as our major workloads: 1. Kapao [13] depicted in Figure 4, a RGB-image-based real-time people key point detection applications used to guide our four-wheeled robot to track and follow a walking people; 2. AGRNav [31] depicted in Figure 3b, an autonomous air-ground robot navigation application that predicts unobserved obstacles by semantic prediction on point clouds and optimizes the navigation trajectory for the air-ground robot. We also verified CacheInf’s performance on a broader range of visual models common to mobile devices: VGGNet [27], ConvNeXt [33], RegNet [35], and we used their default implementation of torchvision [29].

Dataset. For AGRNav we used the officially available sequence of point clouds input [31] and for Kapao, we used the Collective Activity Dataset (CAD) [4] which are sequences of video images of people doing different activities captured using hand-held cameras. For the rest of the models from torchvision, we used the DAVIS [20] dataset which are sequences of video images of different objectives captured also using hand-held cameras.

Experiment Environments. The experiments across all systems and all workloads were conducted in two different real-world environments: 1. indoors, where the robot was moving in our office with desks and separators interfering wireless bandwidth; 2. outdoors, where the robot was moving in a garden with trees and bushes interfering with wireless signals and less reflection, resulting in lower bandwidth. The bandwidth fluctuation of each of the environments are shown in Fig. 1.

Baselines. We selected two SOTA inference acceleration methods as baselines: DSCCS [9] (referred to as DS), which searches for optimal layer partition strategy of a visual model to offload layers to the GPU server to accelerate inference, and Hybrid-Parallel [28] (referred to as HP), which enables parallelization of local computation and offloading by also partitioning the layer input / output of local operators besides layer partitioning to further accelerate inference. We also combined DSCCS with our cache mechanism (referred to as DS-C) to present another perspective about CacheInf’s performance gain. We refer to CacheInf as Ours in the tables. Each result in the tables is followed with standard deviation ($\pm n$).

The evaluation questions are as follows:

- RQ1: How much does CacheInf benefit real-world robotic applications by reducing inference time and energy consumption?
- RQ2: How does CacheInf perform on more models common to mobile devices?
- RQ3: How is the above gain achieved in CacheInf and what affects it?
- RQ4: What are the limitations and potentials of Cache-Inf?

6.2 End-to-End Performance on Real-World Applications

Table 1 shows the end-to-end inference latency and the ratio that transmission time takes up the inference latency and compared with the baselines (we include results of local computation (referred to as Local) for comparison). CacheInf reduced inference latency by 35.5% to 44.4% indoors and 29.4% to 40.0% outdoors for Kapao and 30.0% to 48.8% indoors and 24.2% to 46.8% outdoors for AGRNav. Compared with HP, while CacheInf reduced transmission time by 6 to 8 ms, CacheInf further reduced inference latency by 8 to 10 ms, confirming the effectiveness of the acceleration of the used sparse local operators. CacheInf’s highest percentage that transmission time takes up the inference latency across all cases shows that with shrunk transmission data volume with cache enabled and the integration of HP, CacheInf tend to offload computation to the GPU server more often. This can also be validated by the increased transmission time and shortened inference latency of DSCCS-C compared with DSCCS.

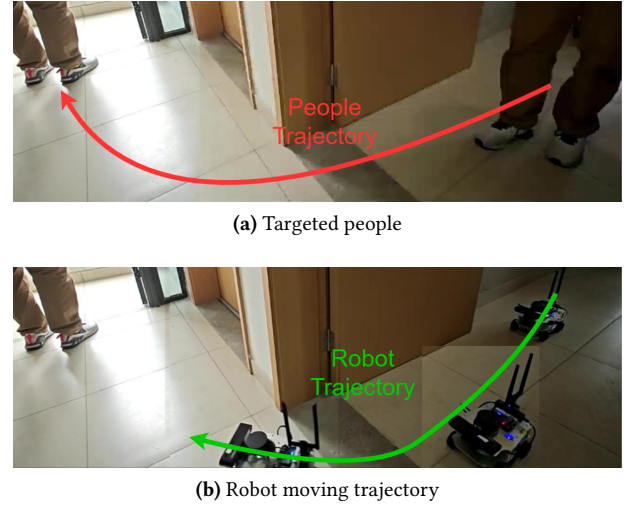


Figure 4. A real-time people-tracking robotic application on our robot based on a state-of-the-art human pose estimation visual model, Kapao [13].

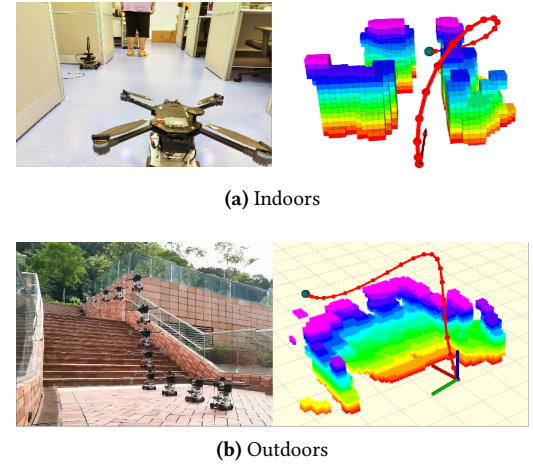


Figure 5. By predicting occlusions in advance, AGRNav [31] gains an accurate perception of the environment and avoids collisions, resulting in efficient and energy-saving paths.

The reduced inference latency of CacheInf leads to reduction of energy consumed per inference by 25.2% to 34.3% indoors and 21.2% to 34.0% outdoors for Kapao and 27.4% to 35.7% indoors and 21.7% to 39.9% outdoors for AGRNav, as shown in Table 2, while the runtime power consumption was increased due to higher frequency of inference.

We report the peak GPU memory consumption on the robot under different strategy in Table 3: CacheInf (includes both the systems of CacheInf and DSCCS-C), No Cache (includes local computation and HP) and Cache All (a naive strategy that caches the output of every layer). The results

Model(number of parameters)	Local computation time/s	System	Transmission time/s		Inference time/s		Percentage(%)	
			indoors	outdoors	indoors	outdoors	indoors	outdoors
Kapao(77M)	1.01(± 0.03)	DS	0.21(± 0.1)	0.24(± 0.12)	0.36(± 0.2)	0.40(± 0.17)	58.33	60.21
		DS-C	0.22(± 0.14)	0.25(± 0.12)	0.32(± 0.25)	0.34(± 0.18)	68.75	73.53
		HP	0.24(± 0.15)	0.28(± 0.13)	0.31(± 0.14)	0.34(± 0.12)	77.42	82.35
		Ours	0.16(± 0.13)	0.21(± 0.18)	0.20(± 0.16)	0.24(± 0.20)	80.09	87.56
AGRNav(0.84M)	0.60(± 0.04)	DS	0.10(± 0.05)	0.15(± 0.05)	0.41(± 0.11)	0.47(± 0.12)	24.39	31.91
		DS-C	0.13(± 0.07)	0.16(± 0.06)	0.38(± 0.10)	0.43(± 0.13)	34.21	37.21
		HP	0.24(± 0.08)	0.26(± 0.07)	0.30(± 0.09)	0.33(± 0.07)	78.65	79.47
		Ours	0.18(± 0.08)	0.20(± 0.08)	0.21(± 0.16)	0.25(± 0.18)	86.71	80.01

Table 1. Average transmission time, inference time, percentage that transmission time accounts for of the total inference time of Kapao and AGRNav in different environments with different systems.

show that CacheInf increased peak GPU memory consumption by 64.6% for Kapao and 58.5% for AGRNav compared with no cache, which is however 72.2% and 81.6% lower than the cases of Cache All, demonstrating the effectiveness of CacheInf’s strategy to reduce the number cached operators.

System	Power consumption(W)		Energy consumption(J) per inference		
	indoors	outdoors	indoors	outdoors	
Kapao	Local	9.91(± 0.49)	9.91(± 0.49)	9.79(± 0.03)	9.79(± 0.03)
	DS	6.38(± 2.21)	6.63(± 2.38)	2.30(± 0.55)	2.65(± 0.55)
	DS-C	6.30(± 2.15)	6.53(± 2.12)	2.02(± 0.50)	2.22(± 0.53)
	HP	7.05(± 1.63)	6.94(± 0.98)	2.19(± 0.62)	2.35(± 0.42)
	Ours	7.53(± 1.62)	7.30(± 0.96)	1.51(± 0.60)	1.75(± 0.41)
AGRNav	Local	8.11(± 0.25)	8.11(± 0.25)	4.86(± 0.01)	4.86(± 0.01)
	DS	6.21(± 1.50)	7.29(± 1.55)	2.55(± 0.19)	3.43(± 0.18)
	DS-C	6.17(± 1.56)	7.00(± 1.43)	2.34(± 0.20)	3.01(± 0.20)
	HP	7.52(± 0.51)	8.04(± 0.45)	2.26(± 0.15)	2.63(± 0.15)
	Ours	7.83(± 0.57)	8.23(± 0.56)	1.64(± 0.17)	2.06(± 0.16)

Table 2. The power consumption against time (Watt) and energy consumption per inference (Joule) of Kapao and AGRNav different environments with different systems.

Model(number of parameters)	Memory Consumption(MB)		
	No Cache	Cache All	CacheInf
Kapao(77M)	300.6	1782.5	494.7
AGRNav(0.84M)	82.8	713.3	131.2

Table 3. Peak GPU memory consumption of different caching strategy on Kapao and AGRNav.

6.3 Performance on Various Common Models

The above conclusions can be further validated by results of a wider range of visual models in Table 4 and Table 5. Across different visual models, CacheInf reduced the inference latency by 13.4% to 43.6% indoors and 13.1% to 45.9% outdoors, and it results in the reduction in energy consumed

per inference to be 11.1% to 46.7% indoors and 9.5% to 42.2% compared with the baselines. Note that although CacheInf’s gain is still evident, the lower bound of CacheInf’s gain decreased on these models compared with Kapao and AGRNav; the reason could be that these models are less computation-intensive, which can be implied from their shorter time for local computation compared with Kapao and AGRNav. When inference of a visual models is not computation-intensive, the gain of using sparse local operators in CacheInf will be limited since execution of each local operator will no longer be the bottleneck. In terms of GPU memory consumption, CacheInf increased GPU memory consumption by 3.2% to 24.8% compared with No Cache, while reducing 12.8% to 39.5% GPU memory consumption compared with Cache All.

6.4 Micro-Event

We first present the micro-events about the real-time inference latency of Kapao of different systems under fluctuating bandwidth in Figure 6. And we can learn that CacheInf consistently achieved the lowest inference latency among all the systems and the gain was most significant under lower bandwidth. Then we fixed the wireless network bandwidth to 48Mb/s and examined different systems’s performance at varied cache ratios from a sequence of video images in Figure 7: at high cache ratios, CacheInf dramatically reduced inference latency compared with other baselines; at low cache ratios, CacheInf degraded to Hybrid-Parallel or even slightly increased inference latency compared with Hybrid-Parallel, and the reason could be the overhead to analyze reusable cache and update cache. We can also observe when cache ratios fluctuated, the inference latency of CacheInf was more stable than DSCCS-C, which can be attributed to CacheInf’s ability to adjust input ratio (x) to reduce inference latency.

6.5 Sensitivity

6.6 Discussion

From the above results we can learn that CacheInf is fundamentally trading-off between GPU memory with inference latency, just as systems in other domains with cache enabled. Since the resulting increased GPU memory consumption

Model(number of parameters)	Local computation time/ms	System	Transmission time/ms		Inference time/ms		Percentage(%)	
			indoors	outdoors	indoors	outdoors	indoors	outdoors
RegNet(54M)	175.0(± 23.6)	DSCCS	47.6(± 47.8)	60.5(± 54.0)	77.8(± 39.3)	86.2(± 37.9)	61.22	70.22
		DSCCS-C	50.7(± 49.8)	62.5(± 53.6)	70.8(± 33.3)	79.5(± 39.2)	71.61	78.61
		HP	49.6(± 21.7)	59.9(± 23.4)	55.0(± 24.8)	64.2(± 25.2)	90.18	93.34
		CacheInf	44.2(± 27.7)	48.5(± 25.3)	45.3(± 35.0)	49.2(± 37.2)	97.57	98.58
VGG19(143M)	118.0(± 18.9)	DSCCS	38.9(± 47.1)	41.6(± 53.8)	65.2(± 28.1)	75.5(± 27.1)	59.75	55.09
		DSCCS-C	42.7(± 30.2)	52.0(± 50.3)	53.2(± 33.0)	60.3(± 30.9)	80.26	86.24
		HP	44.8(± 20.9)	51.5(± 15.0)	47.6(± 18.1)	53.6(± 14.7)	94.15	96.07
		CacheInf	37.8(± 31.2)	43.5(± 13.2)	41.1(± 20.3)	46.6(± 12.8)	94.26	93.34
ConvNeXt(197M)	316.7(± 31.0)	DSCCS	56.0(± 36.1)	67.0(± 37.6)	79.2(± 35.9)	90.6(± 35.4)	70.72	73.98
		DSCCS-C	56.0(± 39.0)	63.0(± 30.2)	64.7(± 40.2)	68.6(± 35.0)	86.55	91.84
		HP	56.4(± 34.7)	66.5(± 33.7)	59.7(± 26.6)	68.0(± 26.6)	94.43	97.88
		CacheInf	40.4(± 37.8)	46.9(± 40.0)	44.7(± 33.3)	49.0(± 30.8)	90.38	95.71

Table 4. Average transmission time, inference time, percentage that transmission time accounts for of the total inference time of common visual models in different environments with different systems.

System	Power consumption(W)		Energy consumption(J) per inference	
	indoors	outdoors	indoors	outdoors
RegNet	9.0(± 0.3)	9.0(± 0.3)	1.37(± 0.02)	1.37(± 0.02)
	5.84(± 1.79)	5.36(± 1.34)	0.45(± 0.14)	0.46(± 0.12)
	6.04(± 1.88)	5.96(± 1.45)	0.43(± 0.16)	0.47(± 0.19)
	5.24(± 1.43)	5.28(± 1.52)	0.29(± 0.08)	0.34(± 0.1)
	5.20(± 1.51)	5.23(± 1.77)	0.24(± 0.08)	0.26(± 0.09)
VGG19	9.78(± 0.34)	9.78(± 0.34)	0.95(± 0.02)	0.95(± 0.02)
	6.58(± 2.14)	6.93(± 2.35)	0.43(± 0.14)	0.52(± 0.18)
	6.82(± 2.10)	7.23(± 2.45)	0.36(± 0.18)	0.43(± 0.30)
	6.51(± 1.74)	7.32(± 1.52)	0.31(± 0.08)	0.39(± 0.08)
	6.70(± 1.88)	7.22(± 1.36)	0.27(± 0.10)	0.34(± 0.09)
ConvNeXt	9.92(± 0.38)	9.92(± 0.38)	3.12(± 0.03)	3.12(± 0.03)
	5.06(± 0.31)	5.02(± 0.37)	0.4(± 0.02)	0.45(± 0.03)
	4.86(± 0.44)	4.99(± 0.39)	0.31(± 0.05)	0.34(± 0.09)
	4.57(± 0.23)	4.54(± 0.25)	0.27(± 0.01)	0.31(± 0.02)
	5.26(± 0.40)	5.39(± 0.27)	0.24(± 0.05)	0.26(± 0.04)

Table 5. The power consumption against time (Watt) and energy consumption per inference (Joule) of common visual models in different environments with different systems.

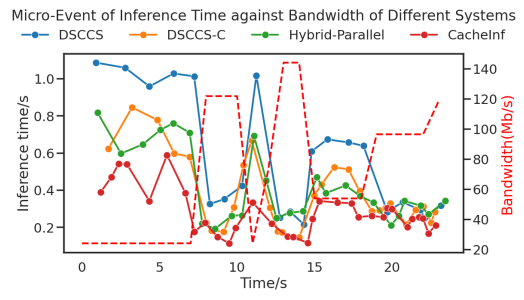


Figure 6. Kapao: inference latency of different systems at different wireless network bandwidth.

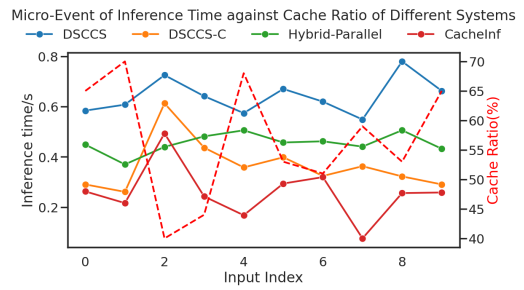


Figure 7. Kapao: inference latency of different systems at different cached ratio with fixed wireless network bandwidth.

Table 6. Peak GPU memory consumption of different caching strategy on common visual models.

may be unfavorable for devices with tight memory budget, adjusting such trade-off to further reduce extra GPU memory consumption to fit in these devices will be our future work.

Another limitation of CacheInf is that it relies on continuity of input and thus is unsuitable for scenarios where the perspective of the robot changes dramatically.

7 Conclusion

In this paper, we present CacheInf, a collaborative edge-cloud cache system for efficient robotic visual model inference. Based on the continuity of visual input of robots in the field and the local operators commonly used in visual models,

Model	Statistics	Difference Filtering Threshold (N)			Chao Ma, Jia-Bin Huang, Xiaokang Yang, and Ming-Hsuan Yang. Hierarchical convolutional features for visual tracking. In <i>Proceedings of the IEEE international conference on computer vision</i> , pages 3074–3082, 2015.
		0.1	0.2	0.3	
Kapao	inference latency accuracy (AP)	75.8	74.6	72.5	[12] Antoni Masiukiewicz. Throughput comparison between the new hew 802.11 ax standard and 802.11 n/ac standards in selected distance windows. <i>International Journal of Electronics and Telecommunications</i> , 65(1):79–84, 2019.
AGRNav	inference latency accuracy ()				[13] William McNally, Kanav Vats, Alexander Wong, and John McPhee. Rethinking keypoint representations: Modeling keypoints and poses as objects for multi-person human pose estimation. In <i>European Conference on Computer Vision</i> , pages 37–54. Springer, 2022.
ConvNeXt	inference latency accuracy ()				[14] NVIDIA. Using Shared Memory in CUDA C/C++. https://developer.nvidia.com/blog/using-shared-memory-cuda-cc/ , January 2013.

Table 7. How different difference filter threshold (N) for identifying reusable cache affects the inference latency of CacheInf and the accuracy of visual models.

we introduce cache mechanism to visual model inference in CacheInf. By reusing computation results of similar local geometries between consecutive inputs, CacheInf accelerates visual model inference by reducing both local computation time and transmission time when offloading computation to the GPU server. The more real-time visual model inference on robots enabled by CacheInf will nurture more visual models to be deployed in real-world robots.

References

- [1] iPerf - Download iPerf3 and original iPerf pre-compiled binaries.
- [2] Toni Adame, Marc Carrascosa-Zamacois, and Boris Bellalta. Time-sensitive networking in ieee 802.11 be: On the way to low-latency wifi 7. *Sensors*, 21(15):4954, 2021.
- [3] Belhassen Bayar and Matthew C Stamm. Constrained convolutional neural networks: A new approach towards general purpose image manipulation detection. *IEEE Transactions on Information Forensics and Security*, 13(11):2691–2706, 2018.
- [4] Wongun Choi, Khurram Shahid, and Silvio Savarese. What are they doing? : Collective activity classification using spatio-temporal relationship among people. In *Proc. of 9th International Workshop on Visual Surveillance (VWS09) in conjunction with ICCV*, 2009.
- [5] Ming Ding, Peng Wang, David López-Pérez, Guoqiang Mao, and Zihua Lin. Performance impact of los and nlos transmissions in dense cellular networks. *IEEE Transactions on Wireless Communications*, 15(3):2365–2380, 2015.
- [6] Reagan L Galvez, Argel A Bandala, Elmer P Dadios, Ryan Rhay P Vicerra, and Jose Martin Z Maningo. Object detection using convolutional neural networks. In *TENCON 2018-2018 IEEE Region 10 Conference*, pages 2023–2027. IEEE, 2018.
- [7] Yuanming Hu, Tzu-Mao Li, Luke Anderson, Jonathan Ragan-Kelley, and Frédéric Durand. Taichi: a language for high-performance computation on spatially sparse data structures. *ACM Trans. Graph.*, 38(6), nov 2019.
- [8] Muyang Li, Ji Lin, Chenlin Meng, Stefano Ermon, Song Han, and Jun-Yan Zhu. Efficient Spatially Sparse Inference for Conditional GANs and Diffusion Models, September 2023. arXiv:2211.02048 [cs].
- [9] Huanghuang Liang, Qianlong Sang, Chuang Hu, Dazhao Cheng, Xiaobo Zhou, Dan Wang, Wei Bao, and Yu Wang. Dnn surgery: Accelerating dnn inference on the edge through layer partitioning. *IEEE transactions on Cloud Computing*, 2023.
- [10] Ruofeng Liu and Nakjung Choi. A first look at wi-fi 6 in action: Throughput, latency, energy efficiency, and security. *Proceedings of the ACM on Measurement and Analysis of Computing Systems*, 7(1):1–25, 2023.
- [11] Chao Ma, Jia-Bin Huang, Xiaokang Yang, and Ming-Hsuan Yang. Hierarchical convolutional features for visual tracking. In *Proceedings of the IEEE international conference on computer vision*, pages 3074–3082, 2015.
- [12] Antoni Masiukiewicz. Throughput comparison between the new hew 802.11 ax standard and 802.11 n/ac standards in selected distance windows. *International Journal of Electronics and Telecommunications*, 65(1):79–84, 2019.
- [13] William McNally, Kanav Vats, Alexander Wong, and John McPhee. Rethinking keypoint representations: Modeling keypoints and poses as objects for multi-person human pose estimation. In *European Conference on Computer Vision*, pages 37–54. Springer, 2022.
- [14] NVIDIA. Using Shared Memory in CUDA C/C++. <https://developer.nvidia.com/blog/using-shared-memory-cuda-cc/>, January 2013.
- [15] NVIDIA. Can Jetson Orin support nccl? - Jetson & Embedded Systems / Jetson Orin NX. <https://forums.developer.nvidia.com/t/can-jetson-orin-support-nccl/232845>, November 2022. Section: Autonomous Machines.
- [16] NVIDIA. The world’s smallest ai supercomputer. <https://www.nvidia.com/en-us/autonomous-machines/embedded-systems/jetson-xavier-series/>, 2024.
- [17] Keiron O’shea and Ryan Nash. An introduction to convolutional neural networks. *arXiv preprint arXiv:1511.08458*, 2015.
- [18] Adam Paszke, Sam Gross, Soumith Chintala, Gregory Chanan, Edward Yang, Zachary DeVito, Zeming Lin, Alban Desmaison, Luca Antiga, and Adam Lerer. Automatic differentiation in pytorch. 2017.
- [19] Yuanteng Pei, Matt W Mutka, and Ning Xi. Connectivity and bandwidth-aware real-time exploration in mobile robot networks. *Wireless Communications and Mobile Computing*, 13(9):847–863, 2013.
- [20] F. Perazzi, J. Pont-Tuset, B. McWilliams, L. Van Gool, M. Gross, and A. Sorkine-Hornung. A benchmark dataset and evaluation methodology for video object segmentation. In *Computer Vision and Pattern Recognition*, 2016.
- [21] PyTorch. Distributed communication package - torch.distributed – PyTorch 2.3 documentation. <https://pytorch.org/docs/stable/distributed.html/>, 2024.
- [22] A Kai Qin, Vicky Ling Huang, and Ponnuthurai N Suganthan. Differential evolution algorithm with strategy adaptation for global numerical optimization. *IEEE transactions on Evolutionary Computation*, 13(2):398–417, 2008.
- [23] Lingyan Ran, Yanning Zhang, Qilin Zhang, and Tao Yang. Convolutional neural network-based robot navigation using uncalibrated spherical images. *Sensors*, 17(6):1341, 2017.
- [24] Waseem Rawat and Zhengui Wang. Deep convolutional neural networks for image classification: A comprehensive review. *Neural computation*, 29(9):2352–2449, 2017.
- [25] Yi Ren, Chih-Wei Tung, Jyh-Cheng Chen, and Frank Y Li. Proportional and preemption-enabled traffic offloading for ip flow mobility: Algorithms and performance evaluation. *IEEE Transactions on Vehicular Technology*, 67(12):12095–12108, 2018.
- [26] Nurul I Sarkar and Osman Mussa. The effect of people movement on wi-fi link throughput in indoor propagation environments. In *IEEE 2013 Tencon-Spring*, pages 562–566. IEEE, 2013.
- [27] Karen Simonyan and Andrew Zisserman. Very deep convolutional networks for large-scale image recognition, 2015.
- [28] Zekai Sun, Xiuxian Guan, Junming Wang, Haoze Song, Yuhao Qing, Tianxiang Shen, Dong Huang, Fangming Liu, and Heming Cui. Hybrid-parallel: Achieving high performance and energy efficient distributed inference on robots, 2024.
- [29] torchvision. torchvision – Torchvision 0.13 documentation. <https://pytorch.org/vision/0.13/>, 2024.
- [30] Bryan Tripp. Approximating the architecture of visual cortex in a convolutional network. *Neural computation*, 31(8):1551–1591, 2019.

- [31] Junming Wang, Zekai Sun, Xiuxian Guan, Tianxiang Shen, Zongyuan Zhang, Tianyang Duan, Dong Huang, Shixiong Zhao, and Heming Cui. Agrnav: Efficient and energy-saving autonomous navigation for air-ground robots in occlusion-prone environments. In *IEEE International Conference on Robotics and Automation (ICRA)*, 2024.
- [32] Panqu Wang, Pengfei Chen, Ye Yuan, Ding Liu, Zehua Huang, Xiaodi Hou, and Garrison Cottrell. Understanding convolution for semantic segmentation. In *2018 IEEE winter conference on applications of computer vision (WACV)*, pages 1451–1460. Ieee, 2018.
- [33] Sanghyun Woo, Shoubhik Debnath, Ronghang Hu, Xinlei Chen, Zhuang Liu, In So Kweon, and Saining Xie. Convnext v2: Co-designing and scaling convnets with masked autoencoders. In *Proceedings of the IEEE/CVF Conference on Computer Vision and Pattern Recognition*, pages 16133–16142, 2023.
- [34] Min Wu, Wanjuan Su, Luefeng Chen, Zhentao Liu, Weihua Cao, and Kaoru Hirota. Weight-adapted convolution neural network for facial expression recognition in human–robot interaction. *IEEE Transactions on Systems, Man, and Cybernetics: Systems*, 51(3):1473–1484, 2019.
- [35] Jing Xu, Yu Pan, Xinglin Pan, Steven Hoi, Zhang Yi, and Zenglin Xu. Regnet: self-regulated network for image classification. *IEEE Transactions on Neural Networks and Learning Systems*, 2022.
- [36] Xinlei Yang, Hao Lin, Zhenhua Li, Feng Qian, Xingyao Li, Zhiming He, Xudong Wu, Xianlong Wang, Yunhao Liu, Zhi Liao, et al. Mobile access bandwidth in practice: Measurement, analysis, and implications. In *Proceedings of the ACM SIGCOMM 2022 Conference*, pages 114–128, 2022.